from the biochemical literature. As of December 1999, this database provides descriptions for 6 archaea, 32 bacteria and 5 eukaryotes. The downloaded data were manually rechecked, removing synonyms and substrates without defined chemical identity.

Construction of metabolic network matrices

Biochemical reactions described within a WIT database are composed of substrates and enzymes connected by directed links. For each reaction, educts and products were considered as nodes connected to the temporary educt–educt complexes and associated enzymes. Bidirectional reactions were considered separately. For a given organism with N substrates, E enzymes and R intermediate complexes the full stoichiometric interactions were compiled into an $(N + E + R) \times (N + E + R)$ matrix, generated separately for each of the 43 organisms.

Connectivity distribution $P(k)$

Substrates generated by a biochemical reaction are products, and are characterized by incoming links pointing to them. For each substrate we have determined k_{in}, and prepared a histogram for each organism, showing how many substrates have exactly $k_{in} = 0,1,....$ Dividing each point of the histogram with the total number of substrates in the organism provided $P(k_{in})$, or the probability that a substrate has k_{in} incoming links. Substrates that participate as educts in a reaction have outgoing links. We have performed the analysis described above for k_{in}, determining the number of outgoing links (k_{out}) for each substrate. To reduce noise logarithmic binning was applied.

Biochemical pathway lengths [$\Pi(l)$]

For all pairs of substrates, the shortest biochemical pathway, $\Pi(l)$ (that is, the smallest number of reactions by which one can reach substrate B from substrate A) was determined using a burning algorithm. From $\Pi(l)$ we determined the diameter, $D = \Sigma_l l \cdot \Pi(l) / \Sigma_l \Pi(l)$, which represents the average path length between any two substrates.

Substrate ranking $\langle r \rangle_o$, $\sigma(r)$

Substrates present in all 43 organisms (a total of 51 substrates) were ranked on the basis of the number of links each had in each organisms, having considered incoming and outgoing links separately ($r = 1$ was assigned for the substrate with the largest number of connections, $r = 2$ for the second most connected one, and so on). This gave a well defined r value in each organism for each substrate. The average rank $\langle r \rangle_o$ for each substrate was determined by averaging r over the 43 organisms. We also determined the standard deviation, $\sigma(r) = \langle r^2 \rangle_o - \langle r \rangle_o^2$ for all 51 substrates present in all organisms.

Analysis of the effect of database errors

Of the 43 organisms whose metabolic network we have analysed, the genomes of 25 have been completely sequenced (5 archaea, 18 bacteria and 2 eukaryotes), whereas the remaining 18 are only partially sequenced. Therefore two main sources of possible errors in the database could affect our analysis: the erroneous annotation of enzymes and, consequently, biochemical reactions (the likely source of error for the organisms with completely sequenced genomes); and reactions and pathways missing from the database (for organisms with incompletely sequenced genomes, both sources of error are possible). We investigated the effect of database errors on the validity of our findings. The data, presented in Supplementary Information, indicate that our results are robust to these errors.

1. Hartwell, L. H., Hopfield, J. J., Leibler, S. & Murray, A. W. From molecular to modular cell biology. *Nature* **402**, C47–52 (1999).
2. Barabási, A.-L. & Albert, R. Emergence of scaling in random networks. *Science* **286**, 509–512 (1999).
3. West, G. B., Brown, J. H. & Enquist, B. J. The fourth dimension of life: fractal geometry and allometric scaling of organisms. *Science* **284**, 1677–1679 (1999).
4. Banavar, J. R., Maritan, A. & Rinaldo, A. Size and form in efficient transportation networks. *Nature* **399**, 130–132 (1999).
5. Albert, R., Jeong, H. & Barabási, A.-L. Error and attack tolerance of complex networks. *Nature* **406**, 378–382 (2000).
6. Ingber, D. E. Cellular tensegrity: defining new rules of biological design that govern the cytoskeleton. *J. Cell Sci.* **104**, 613–627 (1993).
7. Bray, D. Protein molecules as computational elements in living cells. *Nature* **376**, 307–312 (1995).
8. McAdams, H. H. & Arkin, A. It's a noisy business! Genetic regulation at the nanomolar scale. *Trends Genet.* **15**, 65–69 (1999).
9. Gardner, T. S., Cantor, C. R. & Collins, J. J. Construction of a genetic toggle switch in *Escherichia coli*. *Nature* **403**, 339–342 (2000).
10. Elowitz, M. B. & Leibler, S. A synthetic oscillatory network of transcriptional regulators. *Nature* **403**, 335–338 (2000).
11. Hasty, J., Pradines, J., Dolnik, M. & Collins, J. J. Noise-based switches and amplifiers for gene expression. *Proc. Natl Acad. Sci. USA* **97**, 2075–2080 (2000).
12. Becskei, A. & Serrano, L. Engineering stability in gene networks by autoregulation. *Nature* **405**, 590–593 (2000).
13. Kirschner, M., Gerhart, J. & Mitchison, T. Molecular 'vitalism'. *Cell* **100**, 79–88 (2000).
14. Barkai, N. & Leibler, S. Robustness in simple biochemical networks. *Nature* **387**, 913–917 (1997).
15. Yi, T. M., Huang, Y., Simon, M. I. & Doyle, J. Robust perfect adaptation in bacterial chemotaxis through integral feedback control. *Proc. Natl Acad. Sci. USA* **97**, 4649–4653 (2000).
16. Bhalla, U. S. & Iyengar, R. Emergent properties of networks of biological signaling pathways. *Science* **283**, 381–387 (1999).
17. Karp, P. D., Krummenacker, M., Paley, S. & Wagg, J. Integrated pathway–genome databases and their role in drug discovery. *Trends Biotechnol.* **17**, 275–281 (1999).
18. Kanehisa, M. & Goto, S. KEGG: Kyoto encyclopedia of genes and genomes. *Nucleic Acids Res.* **28**, 27–30 (2000).
19. Overbeek, R. *et al.* WIT: integrated system for high-throughput genome sequence analysis and metabolic reconstruction. *Nucleic Acids Res.* **28**, 123–125 (2000).
20. Erdös, P. & Rényi, A. On the evolution of random graphs. *Publ. Math. Inst. Hung. Acad. Sci.* **5**, 17–61 (1960).
21. Bollobás, B. *Random Graphs* (Academic, London, 1985).
22. Albert, R., Jeong, H. & Barabási, A.-L. Diameter of the World-Wide Web. *Nature* **400**, 130–131 (1999).
23. Faloutsos, M., Faloutsos, P. & Faloutsos, C. On power-law relationships of the internet topology. *Comp. Comm. Rev.* **29**, 251 (1999).
24. Amaral, L. A. N., Scala, A., Barthelemy, M. & Stanley, H. E. Classes of behavior of small-world networks. (cited 31 January 2000) 〈http://xxx.lanl.gov/abs/cond-mat/0001458〉 (2000).
25. Dorogovtsev, S. N. & Mendes, J. F. F. Evolution of reference networks with aging (cited 28 January 2000) 〈http://xxx.lanl.gov/abs/cond-mat/0001419〉 (2000).
26. Watts, D. J. & Strogatz, S. H. Collective dynamics of 'small-world' networks. *Nature* **393**, 440–442 (1998).
27. Barthelemy, M. & Amaral, L. A. N. Small-world networks: Evidence for a crossover picture. *Phys. Rev. Lett.* **82**, 3180–3183 (1999).
28. Edwards, J. S. & Palsson, B. O. The *Escherichia coli* MG1655 *in silico* metabolic genotype: its definition, characteristics, and capabilities. *Proc. Natl Acad. Sci. USA* **97**, 5528–5533 (2000).

Correspondence and requests for materials should be addressed to A.-L.B. (e-mail: alb@nd.edu) or Z.N.O. (e-mail: zno008@northwestern.edu).

....

errata

Determining multiple length scales in rocks

Yi-Qiao Song, Seungoh Ryu & Pabitra N. Sen

On page 179 of this paper, the six occurrences of $\pi 2$ on lines 10 and 23 of the text should have been $\pi/2$. ☐

Glycosyltransferase activity of Fringe modulates Notch–Delta interactions

Katja Brücker, Lidia Perez, Henrik Clausen & Stephen Cohen

In Fig. 1b, the fifth column of the Fng–myc row should have shown a plus sign instead of a minus sign. ☐

letters to nature

Most samples give 28–33% O_2 yield during laser fluorination. We found by analysing NBS127 (NIST sulphate standard), seawater sulphate, and a low-$\delta^{18}O$ in-house standard that the raw $\delta^{18}O$ values are consistently 9.4 lower than the reported ones, owing to the incomplete O_2 generation. The correction factor is also verified by more than a dozen natural sulphate samples—that have been analysed using both the laser-fluorination method and the graphite reduction/CO_2-fluorination method[27]—that normally reach a 85% to 100% O_2 yield in our laboratory. This comparison also verifies that the incomplete O_2-generation using a CO_2-laser does not deviate from the slope of 0.52. Thus, the reported $\delta^{17}O$ value is increased by 4.89‰. $\delta^{34}S$ was analysed using the SF_6 method[28]. In this report, all $\Delta^{17}O$ values are calculated on the basis of raw $\delta^{17}O$ and $\delta^{18}O$ values. We use the linear equation to calculate $\Delta^{17}O$ because all the raw $\delta^{17}O$ and $\delta^{18}O$ values are close to the vicinity of the origin and the range of $\delta^{17}O$ and $\delta^{18}O$ values among different samples are small.

1. Clayton, R. N., Grossman, L. & Mayeda, T. K. A component of primitive nuclear composition in carbonaceous chondrites. *Science* **182**, 485–488 (1973).
2. Matsuhisa, Y., Goldsmith, J. R. & Clayton, R. N. Mechanisms of hydrothermal crystallization of quartz at 250 degrees C and 15 kilobars. *Geochim. Cosmochim. Acta* **42**, 173–182 (1978).
3. Thiemens, M. H. Atmosphere science—Mass-independent isotope effects in planetary atmospheres and the early solar system. *Science* **283**, 341–345 (1999).
4. Robert, F., Rejou-Michel, A. & Javoy, M. Oxygen isotropic homogeneity of the Earth: new evidence. *Earth Planet. Sci. Lett.* **108**, 1–9 (1992).
5. Clayton, R. N. & Mayeda, T. K. Oxygen isotope studies of achondrites. *Geochim. Cosmochim. Acta* **60**, 1999–2017 (1996).
6. Farquhar, J., Thiemens, M. H. & Jackson, T. Atmosphere-surface interactions on Mars: Delta O-17 measurements of carbonate from ALH 84001. *Science* **280**, 1580–1582 (1998).
7. Mauersberger, K. Ozone isotope measurements in the stratosphere. *Geophys. Res. Lett.* **14**, 80–83 (1987).
8. Krankowsky, D., Bartecki, F., Klees, G. G., Mauersberger, K. & Schellenbach, K. Measurement of heavy isotope enrichment in tropospheric ozone. *Geophys. Res. Lett.* **22**, 1713–1716 (1995).
9. Johnston, J. C. & Thiemens, M. H. The isotopic composition of tropospheric ozone in three environments. *J. Geophys. Res.* **102** (D21), 25395–25404 (1997).
10. Savarino, J. & Thiemens, M. H. Analytical procedure to determine both delta O-18 and delta O-17 of H_2O_2 in natural water and first measurements. *Atmos. Environ.* **33**, 3683–3690 (1999).
11. Lee, C. W. Multiple stable oxygen isotopic studies of atmospheric sulfate aerosols. *Am. Geophys. Union* **78**, F111 (1997).
12. Lee, C. W., Savarino, J. & Thiemens, M. H. Multiple stable oxygen isotopic studies of sulfate and hydrogen peroxide collected from rain water: a new way to investigate in-situ S(IV) oxidation chemistry by dissolved H_2O_2 in aqueous solution. *Am. Geophys. Union* **79**, F91 (1998).
13. Eckardt, F. D. & Spiro, B. The origin of sulphur in gypsum and dissolved sulphate in the Central Namib Desert, Namibia. *Sedim. Geol.* **123**, 255–273 (1999).
14. Siesser, W. G. Late Miocene origin of the Benguela upwelling system off northern Namibia. *Science* **208**, 283–285 (1980).
15. Armstrong, R. L. & Ward, P. L. Evolving geographic patterns of Cenozoic magmatism in the North American Cordillera; the temporal and spatial association of magmatism and metamorphic core complexes Mid-Tertiary Cordilleran magmatism; plate convergence versus intraplate processes. *J. Geophys. Res. B* **96**, 13201–13224 (1991).
16. Nicknish, J. M. & Macdonald, J. R. Basal Miocene ash in White River Badlands, South Dakota. *Bull. Am. Assoc. Petrol. Geol.* **46**, 685–690 (1962).
17. Swisher, C. C. III. *Stratigraphy And Biostratigraphy Of The Eastern Portion Of Wildcat Ridge, Western Nebraska.* Thesis, Univ. Nebraska (1982).
18. Rose, W. I. Jr, Chuan, R. L., Cadle, R. D. & Woods, D. C. Small particles in volcanic eruption clouds. *Am. J. Sci.* **280**, 671–696 (1980).
19. Gamsjäger, H. & Murmann, R. K. in *Advances in Inorganic and Bioinorganic Mechanisms* (ed. Sykes, A. G.) 317–381 (Academic, London, 1983).
20. Cerling, T. E. Carbon dioxide in the atmosphere – evidence from Cenozoic and Mesozoic paleosols. *Am. J. Sci.* **291**, 377–400 (1991).
21. Rye, R. & Holland, H. D. Paleosols and the evolution of atmospheric oxygen: A critical review. *Am. J. Sci.* **298**, 621–672 (1998).
22. Berner, R. A. *et al.* Isotope fractionation and atmospheric oxygen: Implications for phanerozoic O_2 evolution. *Science* **287**, 1630–1633 (2000).
23. Karlsson, H. R., Clayton, R. N., Gibson, E. K. & Mayeda, T. K. Water in SNC meteorites - Evidence for a martian hydrosphere. *Science* **255**, 1409–1411 (1992).
24. Farquhar, J. & Thiemens, M. H. The oxygen cycle of the Martian atmosphere-regolith system: $\Delta^{17}O$ of secondary phases in Nakhla and Lafayette. *J. Geophys. Res.* **105** (E5), 11991–11997 (2000).
25. Bao, H. & Thiemens, M. H. Generation of O_2 from $BaSO_4$ using a CO_2-laser fluorination system for simultaneous $\delta^{18}O$ and $\delta^{17}O$ analysis. *Anal. Chem.* (in the press).
26. Clayton, R. N. & Mayeda, T. K. Oxygen isotopes in eucrites, shergottites, nakhlites, and chassignites. *Earth Planet. Sci. Lett.* **62**, 1–6 (1983).
27. Bhattacharya, S. K. & Thiemens, M. H. New evidence for symmetry dependent isotope effects - O+CO reaction. *Z. Naturforsch. A J. Phys. Sci.* **44**, 435–444 (1989).
28. Forrest, J. & Newman, L. Silver-110 microgram sulfate analysis for the short time resolution of ambient level of sulfur aerosol. *Anal. Chem.* **49**, 1579–1584 (1977).

Determining multiple length scales in rocks

Yi-Qiao Song, Seungoh Ryu & Pabitra N. Sen

Schlumberger-Doll Research, Old Quarry Road, Ridgefield, Connecticut 06877, USA

Carbonate reservoirs in the Middle East are believed to contain about half of the world's oil[1]. The processes of sedimentation and diagenesis produce in carbonate rocks microporous grains and a wide range of pore sizes, resulting in a complex spatial distribution of pores and pore connectivity[2]. This heterogeneity makes it difficult to determine by conventional techniques the characteristic pore-length scales, which control fluid transport properties. Here we present a bulk-measurement technique that is non-destructive and capable of extracting multiple length scales from carbonate rocks. The technique uses nuclear magnetic resonance to exploit the spatially varying magnetic field inside the pore space itself—a 'fingerprint' of the pore structure. We found three primary length scales (1–100 μm) in the Middle-East carbonate rocks and determined that the pores are well connected and spatially mixed. Such information is critical for reliably estimating the amount of capillary-bound water in the rock, which is important for efficient oil production. This method might also be used to complement other techniques[3–5] for the study of shaly sand reservoirs and compartmentalization in cells and tissues.

Nuclear magnetic resonance (NMR) is often used to investigate porous media by applying external magnetic field gradients in a fashion analogous to X-ray diffraction in determining the size of cells[6] and pores[7–9]. In fact, when a sample is placed in a uniform magnetic field, a spatially varying field and its gradients appear naturally inside the pore space as a result of the magnetic susceptibility contrast between the host solid material and the pore-filling fluid[10]. This field is called the internal field, B^i, and it can be large enough in natural materials such as rocks[11–14] to interfere with the
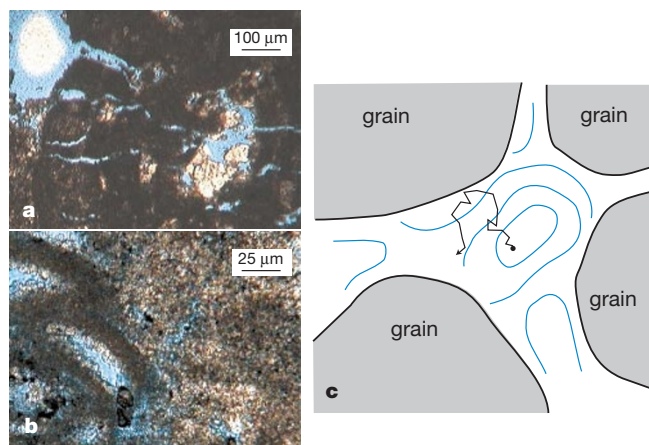

Figure 1 Thin-section micrographs of the pore space in Thamama carbonate rocks and an illustration of the internal magnetic field. **a**, **b**, The blue regions are pores filled with blue epoxy before sectioning. Pores of size a few μm to about 100 μm are clearly visible. The smaller pores show up as different level of shades owing to limited resolution. It is crucial to determine these length scales in understanding the transport properties. **c**, Diagram of the typical pore space, internal magnetic field B^i and diffusion. The blue lines illustrate the constant B^i_z contours (the component along the external field) reflecting the local pore geometry. The magnetization decay due to diffusion in B^i is used to characterize the pore sizes.
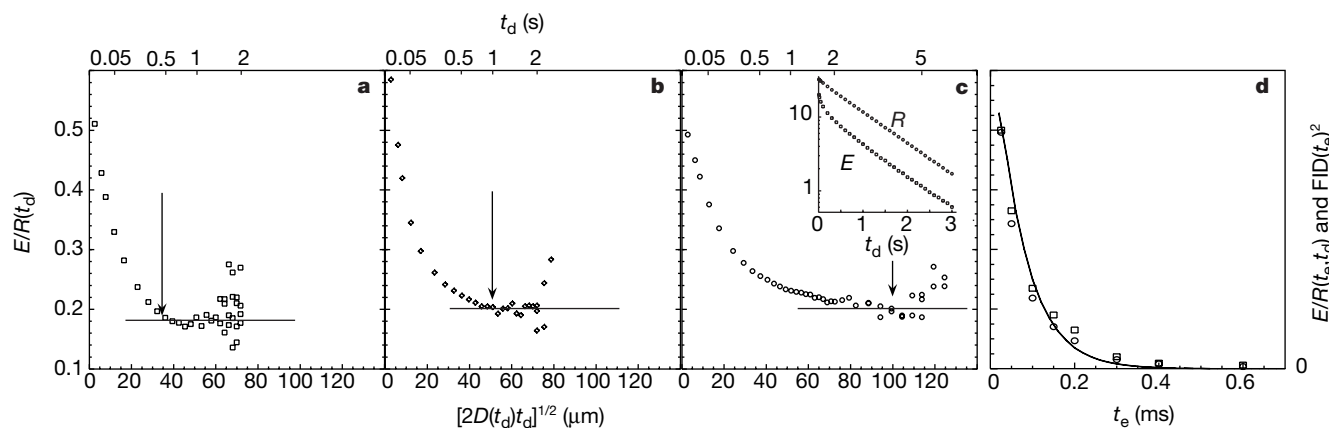
Figure 2 Experimental results on uniform-size, randomly-packed glass bead samples saturated with water. **a**–**c**, The DDIF ratio (E/R) as a function of the r.m.s. displacement, that is, $(2D(t_d)t_d)^{1/2}$, of water molecules calculated for each bead size using the formula in ref. 19. The corresponding t_d is shown at the top of the graphs. The average diameters are: **a**, 30.6; **b**, 50; and **c**, 105 μm. The initial decay and eventual constant DDIF ratio is clear for all samples. The inset in **c** shows the echo (E) and the reference signals (R) for the 100-μm bead sample. **d**, The DDIF ratio as a function of t_e for the 30-μm bead sample, at $t_d = 0.4$ s (squares) and 1 s (circles) which correspond to r.m.s. displacements of 32 and 50 μm respectively. The line is the square of the FID, consistent with equation (3). NMR experiments were performed on a Tecmag spectrometer at a magnetic field of 2.14 T.

applied gradients. B^i is determined by the spatial distribution of pores and thus reflects the detailed pore structure, shown in Fig. 1. We have developed a new NMR technique to characterize B^i in order to study the complex pore geometry in carbonate rocks. We will first describe the essential concept of this method, demonstrate its utility using samples of known sizes, and then apply it to natural rocks.

We use water protons to probe B^i as they diffuse in the pore space, by measuring the ^{1}H magnetization diffusion with the stimulated echo pulse sequence[15]: $\frac{\pi}{2} - t_e - \frac{\pi}{2} - t_d - \frac{\pi}{2} - t_e - $ echo. Here, t_d is the diffusion times and t_e is the echo time. The notation $\pi/2$ denotes a radio-frequency pulse that rotates the spin vector by 90°. For $t_e \ll t_d$, diffusion during t_e may be neglected. The normalized echo intensity, E, measure the change in B^i as protons diffuse during t_d (ref. 10):

$$E(t_e, t_d) = \int d\mathbf{x}_1 d\mathbf{x}_2 e^{i\gamma t_e [B_z^i(\mathbf{x}_1) - B_z^i(\mathbf{x}_2)]} \cdot P(\mathbf{x}_1, \mathbf{x}_2, t_d) \quad (1)$$

where γ is the ^{1}H gyromagnetic ratio. B_z^i is the component of B^i along the external field, $\mathbf{x}_1$ and $\mathbf{x}_2$ are the initial and the final positions and $P(\mathbf{x}_1, \mathbf{x}_2, t_d)$ is the diffusion propagator for the magnetization density[10]. No external field gradient is applied.

The additional decay of E due to spin-lattice relaxation (T_1) can be calibrated by the reference signal, $R(t_e, t_d)$, obtained in: $\frac{\pi}{2} - t_e - \pi - t_e - \frac{\pi}{2} - t_d - \frac{\pi}{2} - $ FID. R is acquired as the initial amplitude of the free-induction decay (FID) signal. The π pulse cancels the phase accumulation due to B^i and thus R is independent of B^i. For the samples considered here, we focus on the decay due to diffusion in the internal field (DDIF) by using the ratio E/R (DDIF ratio) to remove the effect of the spin-lattice relaxation.

Experimental results using random-packed bead samples (Duke Scientific Co.) are shown in Fig. 2. For all samples, the DDIF ratio shows a progressive decay as a function of t_d, at short t_d. This decay is caused by the change of B^i for each diffusing spin, $\langle [B_z^i(\mathbf{x}_1) - B_z^i(\mathbf{x}_2)]^2 \rangle \neq 0$, similar to the case of applied field gradients[15]. However, the decay rate reduces as t_d lengthens, and eventually, for all bead sizes, the DDIF ratio becomes constant at long t_d. This time-dependent behaviour can be used to define a critical time t_c as the time when the decay rate approaches zero. The corresponding diffusion length is indicated by the arrows in Fig. 2a–c and it corresponds well to the bead diameter of the individual sample.

To understand the long-time asymptote of the t_d-independent signal, equation (1) may be rewritten in terms of the magnetic field

B, neglecting spin relaxation:

$$E(t_e, t_d) = \int_{B_{min}}^{B_{max}} dB_1 dB_2 f(B_1) f(B_2) \times e^{i\gamma t_e [B_1 - B_2]} \cdot \tilde{P}(B_1, B_2, t_d) \quad (2)$$

where $f(B)$ is the distribution of B^i and $\tilde{P}(B_1, B_2, t)$ is the propagator in B^i space. However, unlike for the applied gradients, it is crucial to realize that B^i is bounded in magnitude and the field variation occurs over the pore-length scale. When the molecule has explored the entire B^i space (at large t_d), B_1 and B_2 become uncorrelated and $\tilde{P}(B_1, B_2, t) \rightarrow 1$:

$$E(t_e, t_d \rightarrow \infty) = \left| \int dB \cdot e^{i\gamma t_e B} f(B) \right|^2 = |\mathrm{FID}(t_e)|^2 \quad (3)$$
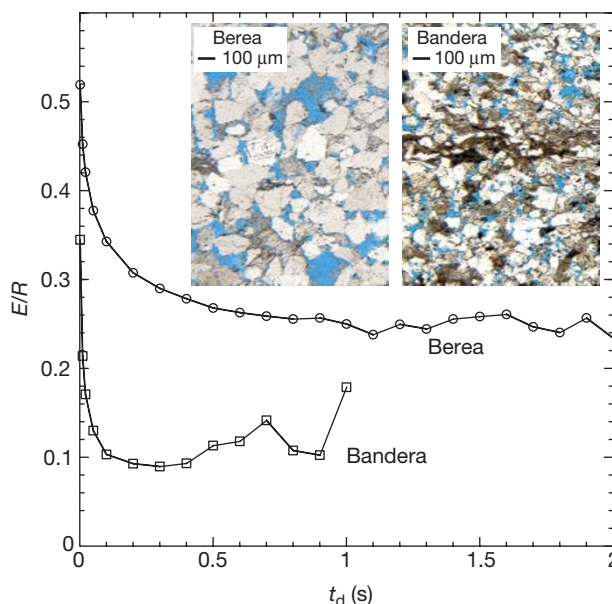

Figure 3 The DDIF ratio for two sandstone samples: Berea 100 and Bandera. Their porosities and permeabilities are: 20% and 260 mD for Berea, 21% and 19 mD for Bandera. The overall trends of the DDIF ratio are very similar except for the decay rate. The pore size L is determined to be 63 and 20 μm for the two samples, respectively. Inset, thin-section images for the two samples. A visual estimate of the pore sizes from the images is consistent with L.

independent of t_d. $E(t_e, t_d \rightarrow \infty)$ equals the square of the FID at time t_e, consistent with the direct measurement of the FID, shown in Fig. 2d. The time (t_c) it takes for the molecule to experience all B^i is related to the length scale L of the field variation, $L \approx \sqrt{2D_0 t_c}$ where D_0 is the bulk diffusion constant. These results demonstrate the utility of t_c (or L) as a direct measure of the characteristic pore dimension.

This unusual time-dependent behaviour can be obtained by a rigorous study of the magnetization diffusion and an outline of such a solution is given here. The decay of the longitudinal magnetization density during t_d is governed by the Bloch-Torrey equation[16,17] which can be solved in terms of eigenmodes (ϕ_n) with characteristic decay time constant T_n for the nth eigenmode. In the fast diffusion limit:

$$R(t_d) \approx e^{-t_d/T_0} \tag{4}$$

$$E(t_d) \approx \alpha_0 e^{-t_d/T_0} + \sum_{n=1}^{\infty} \alpha_n e^{-t_d/T_n} \tag{5}$$

The coefficients are determined by $B_z^i(x)$: $\alpha_n = |\int dx \phi_n(x) e^{i\gamma_e B_z^i(x)}|^2 / \int \phi_n(x)^2 dx$. Brownstein and Tarr[17] showed that the spatially uniform initial magnetization commonly used in relaxation measurements ensures that the decay is dominated by the lowest mode with the time constant T_0. On the other hand, the presence of B^i changes the spatial magnetization profile at the beginning of the t_d period to something mimicking B^i that is not uniform on the pore-length

scale, which thus increases the weight of the higher modes in E. The T_n of such high modes are directly related to the pore sizes, for example, $L = n\pi \sqrt{D_0 T_n}$ for spherical pores. Thus, the enhanced faster-decaying modes in $E(t_d)$ in comparison with $R(t_d)$ may be used to determine pore size, using an inverse Laplace transform. In the case where $R(t_d)$ is approximately exponential, the ratio $E(t_d)/R(t_d)$ can be used directly to determine pore sizes via the inverse Laplace transform.

DDIF measurements for two sandstone rocks are shown in Fig. 3 with the cross-section micrographs of the pore space. The DDIF ratio shows very similar behaviour to that of the packed bead samples: with pronounced initial decay and eventual saturation. The different decay rates are indicative of the different pore size and L was evaluated to be 63 and 20 μm, respectively, consistent with the estimated pore sizes from the micrographs (insets of Fig. 3).

We have studied several carbonate rocks from the Thamama formation of the Middle East. The representative DDIF behaviour, shown in Fig. 4a, is strikingly different from that of the previous sandstone samples. The initial DDIF decay occurs over a very short time period of up to 10 ms. This decay is dominated by water diffusing within pores of the size $\sqrt{2D_0 t_c} \approx 6$ μm ($D_0 \approx 2 \times 10^{-5}$ cm^2 s^{-1} at 20 °C), that is, the micropore length scale. After the initial reduction, the decay of the DDIF ratio slows down dramatically and continues to 3 s, owing to a larger dimension of the pore space, 10^2 μm. This data shows directly the presence of two distinct length scales associated with the micropores and the macropores of the sample. Further analysis of the DDIF ratio, using a numerical inverse Laplace transform, yields the pore-size distribution function, shown in the inset of Fig. 4a, suggesting two sub-populations of pores of 3 and 13 μm sizes, in the microporosity region corresponding to intragranular and intergranular pores. A similar range of pore sizes is also observed on the surface using electron and optical microscopy results (Fig. 1a and b).

The T_1 relaxation data for the sample is illustrated in the Fig. 4b and the T_1 distribution (inset) shows a single narrow peak. This apparently homogeneous behaviour indicates that the pore size heterogeneity, present in the DDIF experiments, must occur within the diffusion length, L_D, which is the distance a proton diffuses during a time of the order $T_1 \approx 1$ s. An order of magnitude estimate of L_D is $\sqrt{6D_0 T_1} \approx 0.1$ mm. In this case, the relaxation method obtains a T_1 averaged over L_D (see ref. 18 for reviews). With the combined results from DDIF and relaxation, we conclude that the multiple pore scales are intimately mixed throughout the entire rock. Thus the transport will be dominated by the intergranular pores and the macropores. Water in micropores (3 μm) is likely to be bound by the capillary pressure during production.

It is of practical importance that the signal loss in DDIF can be made very small, that is a 10–20% decay in E, in contrast to the two orders of magnitude loss of signal in conventional pulsed field gradient experiments[7]. In addition, since only radio-frequency pulses are used without pulsed field gradients, the minimum accessible diffusion time can be microseconds, extending the range of the detectable length scale to 0.1–100 μm using water. Taking advantage of the ubiquitous internal field in materials[10–14], this technique may find use in the *in situ* characterization of sedimentary rocks, cements and concretes, and also cells and compartmentalization in biological media. □
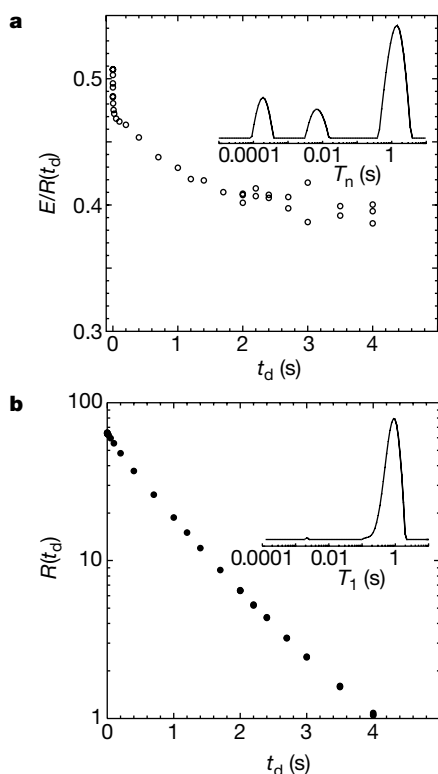

Figure 4 DDIF and relaxation measurements on a Thamama carbonate rock. The porosity and the permeability of the sample are: 23% and 4 mD. **a**, The DDIF ratio and the distributions of diffusion modes T_n (inset). The DDIF ratio versus t_d shows two distinct regimes: very fast decay up to 10 ms and a much slower decay up to 3 s, evidence of the two distinct length scales (a few μm and ~100 μm). The inset shows three populations of pores corresponding the intragranular and intergranular pores and macropores. **b**, The reference signals (R) measured at the same t_d values as for **a** and the distribution of T_1 (inset). The narrow T_1 distribution indicates significant diffusion between the pores over the T_1 timescale. For both experiments, the t_d data consists of 35 points and 10 points below 20 ms.

1. *World Oil Trends* (Arthur Andersen and Cambridge Energy Research Associates, 1997).
2. Tucker, M. E. *Sedimentary Petrology* 2nd edn (Blackwell, Oxford, 1991).
3. Wong, P. Z. (ed.) *Methods in the Physics of Porous Media* (Academic Press, London, 1999).
4. Kleinberg, R. L. in *Encyclopedia of Nuclear Magnetic Resonance* (eds Grant, D. M. & Harris, R. K.) Vol. 8, 4969 (Wiley, New York, 1996).
5. Kenyon, . E. Nuclear magnetic resonance as a petrophysical measurement. *Nucl. Geophys.* **6**, 153–171 (1992).
6. Cory, D. G. & Garroway, A. N. Measurement of translational displacement probabilities by NMR: An indication of compartmentation. *Magn. Reson. Med.* **14**, 435–444 (1990).

180 NATURE | VOL 406 | 13 JULY 2000 | www.nature.com

7. Callaghan, P. T., Coy, A., MacGowan, D., Packer, K. J. & Zelaya, F. O. Diffraction-like effects in NMR diffusion studies of fluids in porous solids. *Nature* **351**, 467–469 (1991).

8. Cotts, R. M. NMR: Diffusion and diffraction. *Nature* **351**, 443–444 (1991).

9. Barrall, G. A., Frydman, L. & Chingas, G. C. NMR diffraction and spatial statistics of stationary systems. *Science* **255**, 714–717 (1992).

10. Callaghan, P. T. *Principles of Nuclear Magnetic Resonance Microscopy* (Oxford Univ. Press, New York, 1993).

11. Hürlimann, M. D. Effective gradients in porous media due to susceptibility differences. *J. Magn. Reson.* **131**, 232–240 (1998).

12. Weisskoff, R. M., Zuo, C. S., Boxerman, J. L. & Rosen, B. R. Microscopic susceptibility variation and transverse relaxation: Theory and experiment. *Magn. Res. Med.* **31**, 601–610 (1994).

13. Borgia, G. C., Brown, R. J. S. & Fantazzini, P. The effect of diffusion and susceptibility differences on T_2 measurements for fluids in porous media and biological tissues. *Magn. Res. Imaging* **14**, 731–736 (1996).

14. Snaar, J. E. M. & Hills, B. P. Constant gradient stimulated echo studies of diffusion in porous materials at high spectrometer fields. *Magn. Res. Imaging* **15**, 983–992 (1997).

15. Hahn, E. L. Spin echoes. *Phys. Rev.* **80**, 580–594 (1950).

16. Torrey, H. C. Bloch equations with diffusion terms. *Phys. Rev.* **104**, 563–565 (1956).

17. Brownstein, K. R. & Tarr, C. E. Importance of classical diffusion in NMR studies of water in biological cells. *Phys. Rev. A* **19**, 2446–2453 (1979).

18. Halperin, W. P., D'Orazio, F., Bhattacharja, S. & Tarczon, J. C. in *Molecular Dynamics in Restricted Geometries* (eds Klafter, J. & Drake, J. M.) Ch. 3 (Wiley, New York, 1989).

19. Latour, L. L., Mitra, P. P., Kleinberg, R. L. & Sotak, C. H. Time-dependent diffusion co-efficient of fluids in porous media as a probe of surface-to-volume ratio. *J. Magn. Res. A* **101**, 342–346 (1993).

....

Cadmium toxicity among wildlife in the Colorado Rocky Mountains

James R. Larison*†, Gene E. Likens‡, John W. Fitzpatrick§ & J. G. Crock‖

* *Section of Ecology and Evolutionary Biology, Cornell University, Ithaca, New York 14853, USA*
‡ *Institute of Ecosystem Studies, Millbrook, New York 12545, USA*
§ *Cornell Laboratory of Ornithology, Ithaca, New York 14850, USA*
‖ *US Geological Survey, Mail Stop 973, Denver Federal Center, Denver, Colorado 80225, USA*

....

Cadmium is known to be both extremely toxic and ubiquitous in natural environments. It occurs in almost all soils, surface waters and plants[1–3], and it is readily mobilized by human activities such as mining[4]. As a result, cadmium has been named as a potential health threat to wildlife species[5]; however, because it exists most commonly in the environment as a trace constituent, reported incidences of cadmium toxicity are rare. Here we have measured trace metals in the food web and tissues of white-tailed ptarmigan (*Lagopus leucurus*) in Colorado. Our results suggest that cadmium toxicity may be more common among natural populations of vertebrates than has been appreciated to date and that cadmium toxicity may often go undetected or unrecognized. In addition, our research shows that ingestion of even trace quantities of cadmium can influence not only the physiology and health of individual organisms, but also the demographics and the distribution of species.

In 1969, C. E. Braun noted the existence of fragile-bone white-tailed ptarmigan (*L. leucurus*) inhabiting the Animas River watershed, near Silverton, Colorado, USA. Because this watershed drains the southwestern corner of the Colorado ore-belt[7], and because this ore-belt region is known to contain high concentrations of a number of potentially toxic trace metals[4], we thought that this fragile-bone condition might be caused by chronic, long-term

exposure to toxic metals, possibly exacerbated by past or present mining operations.

Between 1997 and 1999, we used multi-metals total analysis[8] to trace metals through the ptarmigan food web within a broad section of southwest and central Colorado. Our studies showed that among all of the trace metals present in the soils and surface waters of this ore-belt region, only two—zinc and cadmium—are accumulated by ptarmigan foods in sufficient quantities to cause potential health affects in birds. Moreover, we found that cadmium is 'biomagnified' by one particular genus of plants, the willows (*Salix* spp.), a common ptarmigan food[9]. All of the species of willow, whether ground hugging or free standing, or whether growing in the alpine or in montane marshes of this region, act as biological pumps, concentrating cadmium by two orders of magnitude above background concentrations (Fig. 1). Mean cadmium concentrations in willow leaf buds and in recently grown shoots and stems were found to be 2.63 $\mu g\,g^{-1}$ on a dry weight basis (range from 0.37 to 10.8 $\mu g\,g^{-1}$). This concentration contrasts sharply with ptarmigan foods belonging to genera other than *Salix*, all of which were found to contain only slightly elevated cadmium concentrations ($n = 5$ species, mean 0.195 $\mu g\,g^{-1}$; range from below detection limits to 0.35 $\mu g\,g^{-1}$). (analysis of variance (ANOVA) *t*-test, $P < 0.0001$). In addition, calcium concentrations were very low (<1%), and noteworthy because such low calcium levels can exacerbate cadmium uptake[10,11].

To determine whether comparably high cadmium concentrations existed in foods actually ingested by ptarmigan, we analysed the crop contents of 13 individual birds and found mean cadmium concentrations of 2.1 $\mu g\,g^{-1}$. These levels were not significantly different from those found in randomly collected samples of willow leaves and leaf buds from the region.

Features of ptarmigan foraging behaviour and wintering distribution appear to affect cadmium exposure rates. First, ptarmigan have been observed in this study, and in at least one other[12], to eat more willow during winter and spring than during the summer months. When other foods, especially *Trifolium* spp., *Bistorta bistorta* and *Geum rossii*, become available (in late spring), ptarmigan switch to these less contaminated foods and, in the process, consume far less cadmium. This expansion of the diet reduces overall cadmium exposure during the summer months. Second, because females tend to over-winter at lower elevations than males[13], and because many of these lowland areas are directly downstream from abandoned mines in Colorado, we suspected that females are exposed to higher cadmium concentrations than males.

Tissue analyses of birds of known age (determined by banding) confirmed that cadmium is accumulated (Fig. 2) at roughly the rate of 0.5 μg per day. At this rate, the average ptarmigan could accumulate toxic concentrations of kidney cadmium after only 600 days of dietary ingestion. The high net uptake rate and the long
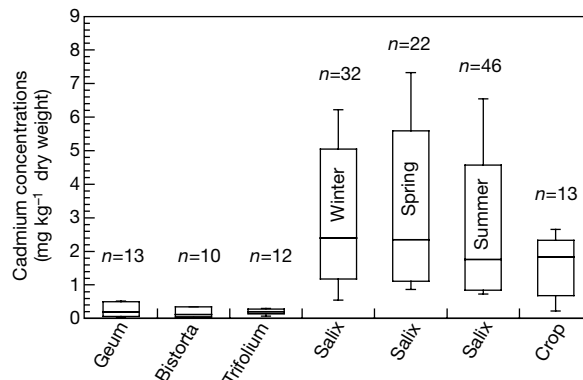

Figure 1 Cadmium concentrations in most commonly eaten ptarmigan foods (genera indicated) and in ptarmigan crops.

Glycosyltransferase activity of Fringe modulates Notch–Delta interactions

Katja Brückner[*][†], **Lidia Perez**[*], **Henrik Clausen**[‡] & **Stephen Cohen**[*]

* *European Molecular Biology Laboratory, Meyerhofstr 1, 69117 Heidelberg, Germany*
‡ *School of Dentistry, University of Copenhagen, Norre Alle 20, Dk2200 Copenhagen N, Denmark*

Ligands that are capable of activating Notch family receptors are broadly expressed in animal development, but their activity is tightly regulated to allow formation of tissue boundaries[1]. Members of the *fringe* gene family have been implicated in limiting Notch activation during boundary formation[2–8], but the mechanism of Fringe function has not been determined. Here we present evidence that Fringe acts in the Golgi as a glycosyltransferase enzyme that modifies the epidermal growth factor (EGF) modules of Notch and alters the ability of Notch to bind its ligand Delta. Fringe catalyses the addition of *N*-acetylglucosamine to fucose, which is consistent with a role in the elongation of *O*-linked fucose *O*-glycosylation that is associated with EGF repeats. We suggest that cell-type-specific modification of glycosylation may provide a general mechanism to regulate ligand–receptor interactions *in vivo*.

In the developing *Drosophila* wing, asymmetric activation of Notch by the dorsally expressed ligand Serrate and the ventrally expressed ligand Delta is required to induce Wingless and Vestigial expression and establish a signalling centre at the dorsal–ventral boundary[9–13]. Fringe is expressed in dorsal cells and contributes to making them more sensitive to Delta and less sensitive to Serrate[2,4,14]. One means by which Fringe might change the sensitivity of dorsal cells to Notch ligands is by modulating ligand–receptor interaction. Alternatively, Fringe might act indirectly to influence cellular signalling responses to a given level of ligand binding. To distinguish between these possibilities, we measured the effect of Fringe on Notch–Delta binding.

We expressed the extracellular domain of Delta as a secreted alkaline phosphatase fusion protein for use in a ligand-binding assay (Delta–AP; Fig 1a). To measure interaction of Delta–AP with transiently transfected *Drosophila* SL2 cells, bound Delta–AP was quantified using an enzymatic assay for alkaline phosphatase activity. Expression levels of the transfected proteins were monitored by immunoblot analysis in parallel to the binding assays. SL2 cells expressing Notch alone or Fringe alone bound Delta–AP at a very low level (Fig 1b). Co-expression of Notch and Fringe resulted in a large increase in the quantity of bound Delta–AP (Fig 1b), even when the level of Notch expression was lower than in the cells expressing Notch alone. The level of proteolytic processing required for formation of a functional receptor was not increased by co-expression of Fringe. This suggests that Fringe activity may increase the ability of Notch-expressing cells to bind Delta.

Although Fringe and its vertebrate homologues can be found as secreted proteins (Fig 2b; refs 2, 15), genetic analysis has suggested that Fringe acts cell-autonomously in the wing disc[11,14]. These apparently contradictory observations prompted us to ask whether secreted Fringe can affect Notch–Delta binding. We compared Delta–AP binding to cells co-expressing Notch and Fringe with its binding to Notch-expressing cells that were co-cultured with Fringe-expressing cells for two days before the binding assay (Fig. 1b). Co-cultured cells bound Delta–AP at background levels. Thus, Fringe does not appear to influence the ability of Notch to

† Present address: Howard Hughes Medical Institute, Department of Genetics, Harvard Medical School, 200 Longwood Avenue, Boston, MA 02115, USA.)

bind Delta when provided as an extracellular protein, but does act when co-expressed with Notch.

The requirement for co-expression of Fringe and Notch could be explained if Fringe exerts its activity within the Notch-expressing cell. Fringe and Brainiac have been suggested to show similarity to bacterial glycosyltransferase enzymes[16], and several mammalian glycosyltransferases related to Brainiac have been characterized[17]. If Fringe functions as a glycosyltransferase enzyme, it should act in the Golgi. To test this possibility, we prepared a Golgi-tethered version of Fringe in which the first 40 amino acids (including the predicted signal peptide) were replaced by the first 121 amino acids of the Golgi-resident glycosyltransferase GalNAc-T3 (Fig 2a; ref. 18). The resulting fusion protein includes the transmembrane domain of GalNAc-T3, which functions as a Golgi-retention signal[19]. Immunoprecipitation from transfected SL2 cells showed that Fringe–GT was expressed at a comparable level to wild-type Fringe, but was not
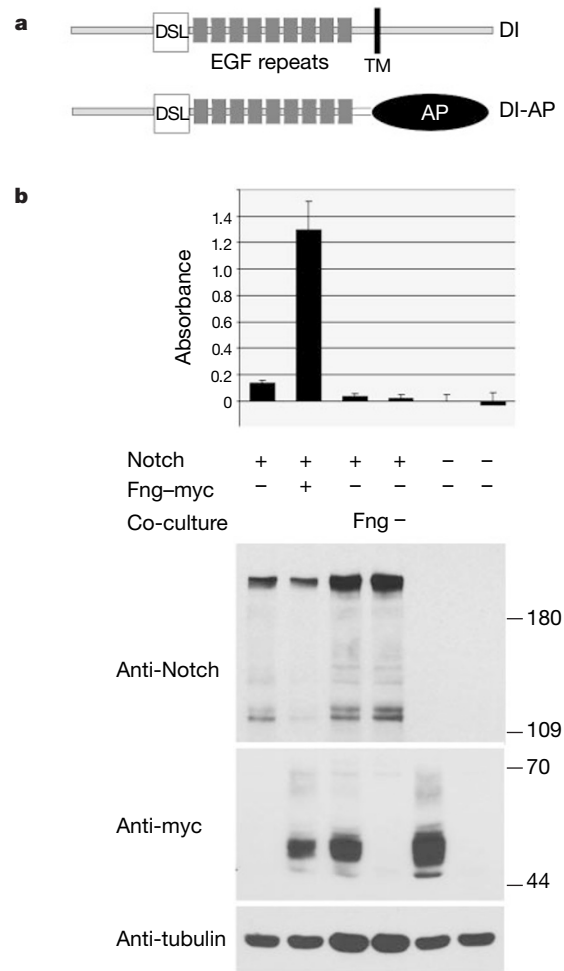

Figure 1 Fringe increases binding of Delta to Notch. **a**, Representation of Delta (Dl) and the secreted Delta–alkaline phosphatase fusion protein. TM, transmembrane domain. DSL, Delta Serrate Lag domain. **b**, Upper panel, Delta–AP binding to control and transfected SL2 cells. Cells were transfected with constructs to direct expression of Notch or Fringe–myc as indicated. Cells transfected with empty vector were used as a control. Co-culture indicates that cells transfected with Notch were grown as a mixed culture with cells independently transfected to express Fringe–myc or with cells transfected with empty vector. AP activity is shown in absorbance units. Means ± s.d. of duplicate binding assays are shown. Lower panels, immunoblots of cell extracts prepared in parallel to those used in the binding assay and probed with anti-Notch, anti-myc and anti-Tubulin. Two forms of Notch are recognized by antibody 9C6. The upper band is the unprocessed form of Notch that does not reach the cell surface[24]; the lower band is the C-terminal portion of the proteolytically processed form, reflecting production of the mature cell-surface protein.

secreted at detectable levels (Fig. 2b). Immunofluorescent labelling of transfected cells with antibody to a Golgi-resident protein and with anti-myc to visualize Fringe–GT–myc showed that the proteins co-localize (Fig. 2c). Together, these observations confirm that the transmembrane tether provided by GalNAc-T3 is effective in SL2 cells.

In binding experiments, co-expression of Fringe–GT was sufficient to stimulate Delta–AP binding to Notch and was almost as effective as wild-type Fringe (Fig. 2d). This suggests that Fringe–GT has comparable activity to wild-type Fringe. Fringe–GT was also found to be functional *in vivo*, despite not being secreted. When expressed under *patched*[GAL4] control Fringe–GT had no effect in the dorsal compartment where endogenous Fringe is expressed, but interrupted the endogenous Wingless stripe at the dorsal–ventral boundary and induced ectopic expression of Wingless in the ventral compartment (Fig. 2e, f). These effects are comparable to those caused by expression of wild-type Fringe–myc (Fig. 2g), and suggest that the Golgi-resident form of Fringe has full biological activity. Many Golgi glycosyltransferase enzymes are also found as secreted soluble enzymes, although the function of the secreted forms is unknown. Therefore, the secretion of Fringe proteins may not be of functional significance to their roles as modifiers of Notch activity.

A D-x-D amino-acid motif found in many glycosyltransferases is required for catalytic activity and appears to be involved in coordination of a divalent metal ion in the binding of the donor nucleotide sugar[16,20,21]. In Fringe, this motif may correspond to residues D236–238. If Fringe acts as a glycosyltransferase, replacing residues 236–238 with asparagine (Fringe-NNN) should destroy enzymatic activity but have a minimal effect on overall protein structure. Consistent with this possibility, co-expression of the Fringe-NNN mutant with Notch did not increase Delta–AP

binding above background levels (Fig. 3a). Furthermore, ectopic expression of Fringe-NNN under *patched*[GAL4] control did not cause Notch activation in the ventral compartment in the wing imaginal disc (not shown). These observations suggest that Fringe-NNN is inactive *in vivo*.

To determine whether Fringe has intrinsic glycosyltransferase activity, we produced wild-type Fringe and Fringe-NNN by baculovirus infection of insect cells. Microsomal fractions enriched for Golgi membranes were partially solubilized and assayed for the ability of the expressed proteins to catalyse the transfer of ^{14}C-labelled UDP donor sugars onto acceptor sugars. We tested a variety of different donor–acceptor combinations (Fig. 3b). The highest level of activity was observed with wild-type Fringe microsome lysate and the combination of UDP-*N*-acetylglucosamine (GlcNAc) and fucose (18-fold over the background level observed with Fringe-NNN). Fringe showed no significant activity with other donor–acceptor combinations.

Fucose is commonly found as an unsubstituted terminal sugar residue in *N*- and *O*-linked oligosaccharide chains of glycoproteins and in glycosphingolipids of eukaryotic cells. In contrast, addition of *O*-linked fucose directly to proteins is a rare type of glycosylation that is found in association with the cysteine-rich consensus sequence C-x-x-G-G-S/T-C (ref. 22). This consensus sequence is found in EGF modules, including a subset of those in Notch, Serrate, Delta, and in their nematode and vertebrate homologues (ref. 23; Fig. 4a). Our results raise the possibility that Fringe functions by elongating *O*-linked fucose residues in the EGF repeats of Notch through the addition of GlcNAc.

To determine whether Fringe acts through the EGF repeats of Notch, we expressed Notch as a fusion protein in which all sequences following the EGF repeats were replaced by heterologous
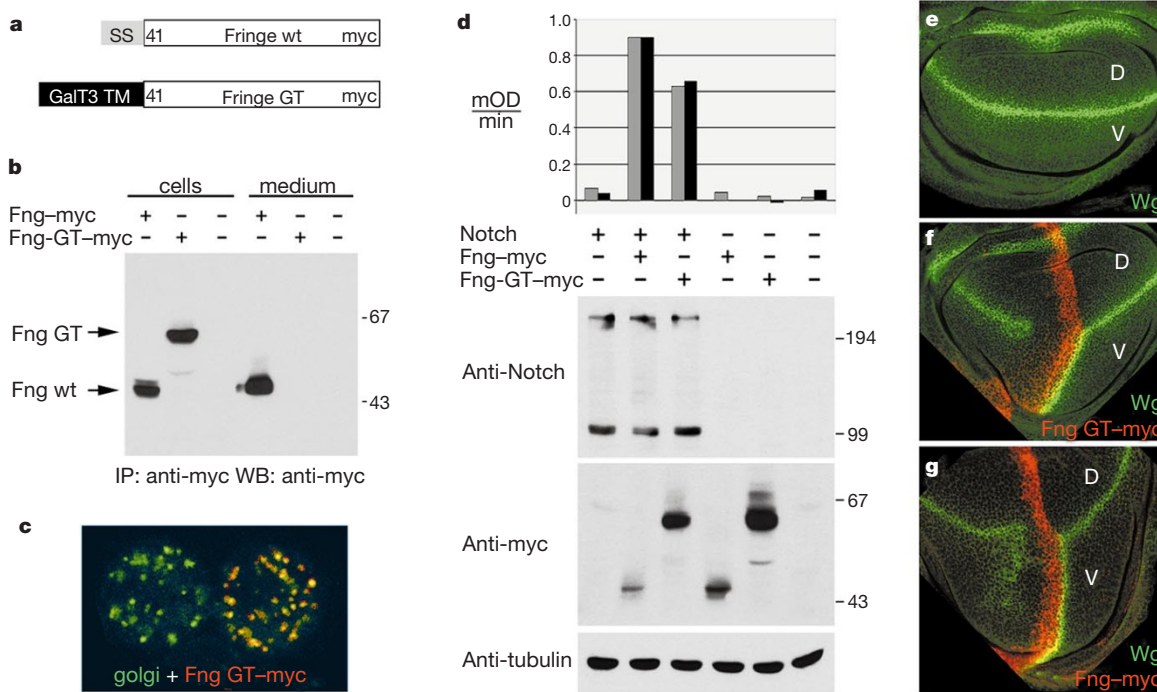

Figure 2 Golgi-tethered Fringe increases binding of Delta to Notch. **a**, Representation of wild-type and Golgi-tethered Fringe (Fng GT). The N-terminal signal sequence (ss) of wild-type fringe (residues 1–40) was replaced by the transmembrane and juxtamembrane region (1–121) of the Golgi-resident GalNAc-T3 protein. Both proteins carry a C-terminal myc tag. **b**, Western blot of myc-tagged proteins immunoprecipitated from whole cell lysates (cells) and from conditioned medium. Cells were transfected to express wild-type Fringe–myc or Fringe–GT–myc. Control cells were transfected with empty vector. **c**, Immunofluorescent labelling of SL2 cells transfected to express Fringe–GT–myc and labelled with antibody to *Drosophila* Golgi (green) and anti-myc (red). The cell on the right

expressed Fringe–GT–myc. **d**, Delta–AP binding to Notch-expressing cells was increased by co-expression of Fringe–myc or Fringe–GT–myc. Replicate experiments are shown. Immunoblots of cell lysates probed with anti-Notch, anti-myc and anti-Tubulin are shown below. **e–g**, Wing imaginal discs labelled to visualize Wingless protein (green) and the myc epitope tag (red). **e**, *patched*[GAL4]/+ control wing disc. D, dorsal compartment; V, ventral compartment. **f**, *patched*[GAL4]/UAS–Fringe–GT–myc. **g**, *patched*[GAL4]/UAS–Fringe–myc. Fringe–GT–myc and wild-type Fringe–myc expression in the *patched*[GAL4] stripe are shown in red.

sequences from the transmembrane protein CD2 (Fig. 4a). Cells expressing Notch–CD2 and Golgi-tethered Fringe–GT bound over 50-fold more Delta–AP than cells expressing Notch–CD2 alone or control cells (Fig. 4b). This observation indicates that the EGF repeats of Notch are sufficient to mediate binding to Delta when taken out of their normal context. Under normal circumstances, expression of Notch on the cell surface requires proteolytic cleavage in the extracellular domain by a furin-like protease[24,25]. The cleaved extracellular domain remains attached to the transmembrane and intracellular domain to form an active receptor complex. In the case of Notch–CD2, proteolytic processing does not appear to be required for cell-surface expression and Delta–AP interaction, as the protein lacks the cleavage site located between Notch–Lin repeats and the transmembrane domain that is used in mouse Notch1.

As the EGF modules of Notch appear to be sufficient to mediate ligand interaction, we reasoned that the corresponding domain of Notch expressed as a soluble AP fusion protein might retain ligand-binding activity (Fig. 4a). We produced Notch–AP in presence or absence of co-expressed Fringe–GT. AP activity of the supernatants was first normalized and binding of the secreted AP fusion proteins was carried out on SL2 cells expressing the full-length form of Delta.
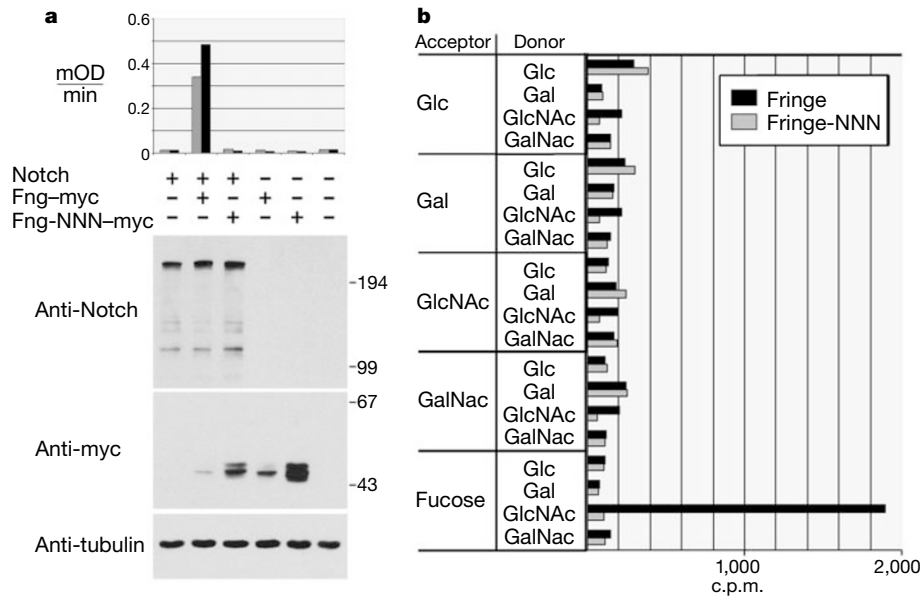

Figure 3 Fringe has glycosyltransferase activity. **a**, Delta–AP binding to control and Notch-transfected SL2 cells. Cells were transfected to express Notch, wild-type Fringe–myc, or mutant Fringe-NNN–myc as indicated. Fringe-NNN–myc has no activity in the binding assay, despite being expressed at higher levels than wild-type Fringe–myc. Lower panels, western blots of cell lysates probed with anti-Notch, with anti-myc and with anti-Tubulin. MOD, absorbance units $\times 10^{-3}$. **b**, Glycosyltransferase activity was measured in microsomal fractions from cells expressing wild-type Fringe–myc or Fringe-NNN–myc. Enzyme activity was measured by transfer of ^{14}C-labelled sugars from UDP donor sugars onto acceptor sugars. Average results from two experiments are shown. Donors tested were UDP-glucose (Glc), UDP-galactose (Gal), UDP-*N*-acetyl-glucosamine (GlcNAc) and *N*-acetyl-galactosamine (GalNAc). Acceptors tested were D-glucose, D-galactose, D-GlcNAc, D-GalNAc and L-fucose.
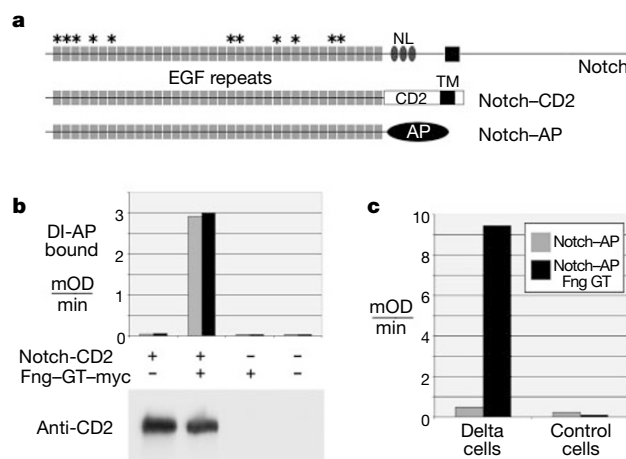

Figure 4 Secreted Notch produced by Fringe–GT-expressing cells binds Delta-expressing cells. **a**, Representation of Notch, Notch–CD2 and the secreted Notch–AP fusion proteins. Notch–CD2 consists of the EGF modules fused to the transmembrane protein CD2. Notch–AP consists of the same EGF modules expressed as a secreted AP fusion protein. Asterisks indicate EGF modules containing a perfect consensus sequence for *O*-linked fucose modification. NL, Notch–Lin repeats; TM, membrane-spanning domain. **b**, Quantitation of Delta–AP binding in replicate experiments. Cells were transfected to express Notch–CD2 or Fringe–GT–myc as indicated. Lower panel, immunoblot probed with anti-CD2. Notch–CD2 expression was comparable in the presence or absence of Fringe–GT–myc. Notch–CD2 lacks the site for furin-mediated cleavage located near the Notch–Lin repeats[25] and migrates at a relative molecular mass of ~200,000. **c**, Quantitation of Notch–AP binding to cells expressing full-length Delta or control cells. Grey bars, Notch–AP produced by SL2 cells; black bars, Notch–AP produced by SL2 cells co-expressing Golgi-tethered Fringe–GT–myc. The level of Notch–AP activity in the conditioned media was normalized.
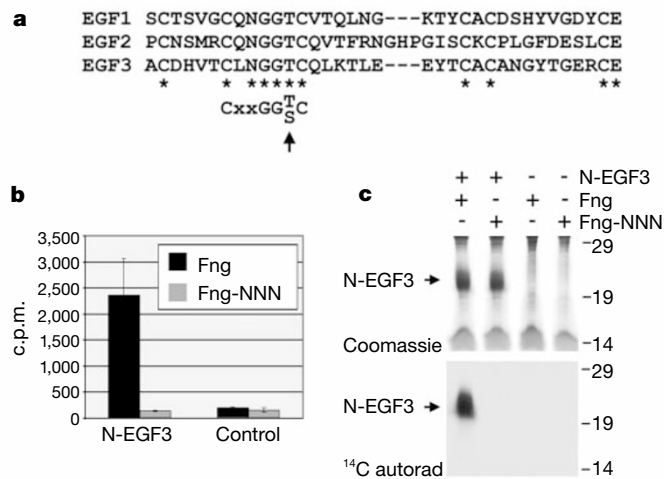
Figure 5 Glycosylation of Notch by Fringe *in vitro*. **a**, Aligned amino-acid sequence of the first three EGF repeats of Notch. Conserved residues and the consensus sequence for *O*-fucosylation are indicated (arrow). **b**, Glycosyltransferase activity of microsomal fractions from cells expressing wild-type Fringe–myc or Fringe-NNN–myc. Enzyme activity was measured by transfer of ^{14}C-labelled UDP-GlcNAc onto Notch–EGF3–His (N-EGF3). Average results from two experiments are shown. **c**, SDS–PAGE of samples from **b** run on a 15% acrylamide gel. Upper panel, Coomassie blue stained gel. The Notch–EGF3 protein is indicated. Lower panel, ^{14}C-UDP-GlcNAc-labelled Notch–EGF3 protein visualized by autoradiography. Background proteins from the microsome fractions were not ^{14}C-labelled.

Notch–AP produced in cells co-expressing Fringe–GT–myc bound to Delta-expressing cells 20 times more effectively than Notch–AP produced in the absence of Fringe (Fig. 4b). This suggests that the observed binding relies solely on the EGF modules of Notch being present as a secreted soluble protein.

To determine whether Fringe acts directly to modify one or more EGF modules of Notch, we carried out an *in vitro* glycosylation assay using a short protein consisting of the first three EGF modules of Notch as the substrate (EGF3). The first three EGF modules of Notch contain perfect consensus sites for addition of *O*-linked fucose (Fig. 5a). The results presented above suggest that Fringe might act by elongating *O*-linked fucose through addition of GlcNAc. The Notch–EGF3 protein was expressed in SL2 cells with a carboxy-terminal histidine tag to permit purification of the secreted protein. Equal amounts of Notch–EGF3 were incubated with ^{14}C-labelled UDP-GlcNAc and microsomal lysates from cells expressing wild-type Fringe or Fringe-NNN. Over 10-fold more labelled GlcNAc was incorporated into Notch–EGF3 by wild-type Fringe than by the mutant form Fringe-NNN (Fig. 5b, c). We conclude that Fringe can act directly to modify the EGF repeats of Notch.

Our results provide evidence that Fringe is a glycosyltransferase enzyme that acts in the Golgi to modify Notch. Fringe-dependent glycosylation of Notch increased its ability to bind Delta. Unexpectedly, we were unable to detect measurable binding of Notch–AP to cells expressing Serrate, or of Serrate–AP to cells expressing Notch. Fringe had no measurable effect on Serrate–AP binding to Notch in our assays when expressed in either the Serrate–AP producing cells or in Notch-expressing cells. This suggests that another factor may be required to promote Notch–Serrate binding. *Drosophila* Brainiac shows limited sequence similarity to Fringe[16] and has been implicated as a modulator of the activities of Notch and EGF signalling pathways[26]. Mammalian Brainiac-related proteins have been characterized as β3Gal or β3GlcNac glycosyltransferases with acceptor substrate specificities distinct from Fringe[17]. It remains to be determined whether Brainiac modifies Notch–ligand or other receptor–ligand interactions.

We propose that Fringe activity determines the type of *O*-linked fucose extension on the EGF repeats of Notch, and possibly on other EGF-repeat-containing proteins. *O*-linked fucose may be extended by the addition of β1-3-glucose or β1-3GlcNAc, and the latter may be followed by addition of galactose and sialic acid residues[22,23]. Our results suggest that Fringe directs elongation of *O*-linked fucose in the EGF modules of Notch by addition of GlcNAc. Fringe-mediated modification changes the properties of Notch–Delta binding and has an important role in conferring signalling specificity *in vivo*. The identification of enzymes that selectively modify oligosaccharide side chains suggests a new range of possibilities for the regulation of ligand–receptor interactions in a cell-type-specific and protein-specific manner. □

Methods

Constructs

Notch–AP was constructed by cloning sequences encoding amino acids 1–1,467 of Notch in frame with human placental alkaline phosphatase from pcDNA3-AP (ref. 27). The fusion junction is located at the *Bsp*EI site between the last EGF repeat and the first Notch–Lin repeat. The same Notch fragment was used to make Notch–CD2 and was linked in frame to rat CD2 at residue 2. For Notch–EGF3, residues GHHHHHH and a stop codon were introduced after residue 177 of Notch. For Delta–AP, a *Bgl*II site was introduced by PCR after residue N592 and sequences encoding residues 1–592 of Delta were fused in frame with AP. For Fringe–myc, residues EFEQKLISEEDL were introduced at the C terminus of Fringe by PCR. Fringe–myc was cloned into pRmHa3 for expression in SL2 cells and into pUAST for GAL4-regulated expression in *Drosophila*. For Fringe-NNN–myc, residues D236–D238 of Fringe–myc were converted to N236–N238 by PCR. For Fringe–GT–myc, fragments encoding the first 121 amino acids of GalNAc-T3 (GenBank accession number X92689) and 40–424 of Fringe–myc were amplified by PCR using oligonucleotides that produce a 15-bp overlapping sequence at the fusion junction. The first two PCR products were used as template to amplify the full-length fusion.

Cell culture and binding assays

Complementary DNAs for expression in *Drosophila* Schneider SL2 cells were cloned into pRmHa3. Cells were transiently transfected by the CaPO₄ method using 4–8 μg of DNA per well in 6-well plates. Expression was induced by addition of 0.7 mM CuSO₄ for 2 days. Conditioned medium was collected from Notch–AP and Delta–AP transfected cells 2–4 days after induction. The activity level of Notch–AP expressed with and without Fringe was normalized by addition of SL2 conditioned medium. AP-containing supernatants were supplemented with 0.1% NaN₃ and incubated with adherent cells for 90 min at room temperature. Cells were washed 5 times with HBSS containing 0.05% BSA and 0.1% azide, and lysed in 10 mM Tris pH 8, 1% Triton-X100. Endogenous AP was inactivated by heat treatment for 10 min at 65 °C and the lysates clarified by centrifugation. AP activity was measured in 1 M diethanolamine, 5 mM MgCl₂, 6.25 mM *p*-nitrophenyl phosphate. Bound AP activity was quantified in 96-well plates using a microplate reader and Micromanager software (BioRad). An additional replicate of each transfection was prepared for immunoblot analysis. Lysates were prepared separately for immunoblot analysis to allow inclusion of protease inhibitors (which were not used in the binding assay).

Glycosyltransferase assays

Fringe–Myc and Fringe-NNN–myc were cloned into baculovirus vector pVL1393

(Pharmingen) and expressed in High Five cells. Microsomal fractions were prepared by hypotonic lysis followed by ultracentrifugation. Membrane pellets were solubilized 1:2 (vol/vol) in 20 mM cacodylate pH 6.5, 1% Triton-CF54 and 5 mM $MnCl_2$ containing leupeptin and aprotinin. This suspension (5 μl) was added to a total of 50 μl reaction mixture containing 25 mM cacodylate pH 6.5, 0.25% Triton-CF54, 5 mM $MnCl_2$, 500 mM free sugar and 100 μM UDP-[^{14}C]sugar (1,280–2,000 c.p.m. nmol^{-1}). Reactions were incubated at 37 °C for 45–60 min, followed by Dowex-1 anion exchange chromatography and scintillation counting of the flow through[28]. For in vitro glycosylation of Notch–EGF3, we transfected SL2 cells and purified secreted His-tagged Notch–EGF3 from conditioned medium by Ni-NTA affinity chromatography. We carried out in vitro glycosylation as described for acceptor sugars using 0.25 μCi [^{14}C]GlcNAc per reaction. After incubation, the Ni-NTA beads were washed 4 times, and labelled Notch–EGF3 protein was eluted with 250 mM imidazole in SDS–PAGE sample buffer.

Immunoprecipitation and western blots

Cells were lysed in 50 mM Tris pH 7.5, 1% TritonX100, 120 mM NaCl and 30 mM NaF, containing protease inhibitors (see ref. 29). Antibodies for immunoprecipitation and western blots included mouse monoclonal anti-Myc (9E10), rabbit anti-Myc (Santa Cruz Biotechnology), mouse anti-CD2 (Serotec) and mouse anti-Notch 9C6. Mouse anti-Golgi (ref. 30). Protein bands were visualized with peroxidase conjugated secondary antibodies and enhanced chemiluminescense (Amersham).

1. Irvine, K. D. Fringe, Notch, and making developmental boundaries. Curr. Opin. Genet. Dev. 9, 434–441 (1999).
2. Panin, V. M., Papayannopoulos, V., Wilson, R. & Irvine, K. D. Fringe modulates Notch–ligand interactions. Nature 387, 908–913 (1997).
3. Johnston, S. H. et al. A family of mammalian Fringe genes implicated in boundary determination and the Notch pathway. Development 124, 2245–2254 (1997).
4. Fleming, R. J., Gu, Y. & Hukriede, N. A. Serrate-mediated activation of Notch is specifically blocked by the product of the gene fringe in the dorsal compartment of the Drosophila wing imaginal disc. Development 124, 2973–2981 (1997).
5. Rodriguez-Esteban, C. et al. Radical fringe positions the apical ectodermal ridge at the dorsoventral boundary of the vertebrate limb. Nature 386, 360–366 (1997).
6. Laufer, E. et al. Expression of Radical fringe in limb-bud ectoderm regulates apical ectodermal ridge formation. Nature 386, 366–373 (1997).
7. Zhang, N. & Gridley, T. Defects in somite formation in lunatic fringe-deficient mice. Nature 394, 374–377 (1998).
8. Evrard, Y. A., Lun, Y., Aulehla, A., Gan, L. & Johnson, R. L. lunatic fringe is an essential mediator of somite segmentation and patterning. Nature 394, 377–381 (1998).
9. Rulifson, E. J. & Blair, S. S. Notch regulates wingless expression and is not required for reception of the paracrine wingless signal during wing margin neurogenesis in Drosophila. Development 121, 2813–2824 (1995).
10. Diaz-Benjumea, F. J. & Cohen, S. M. Serrate signals through Notch to establish a Wingless-dependent organizer at the dorsal/ventral compartment boundary of the Drosophila wing. Development 121, 4215–4225 (1995).
11. Kim, J., Irvine, K. D. & Carroll, S. B. Cell recognition, signal induction and symmetrical gene activation at the dorsal/ventral boundary of the developing Drosophila wing. Cell 82, 795–802 (1995).
12. Doherty, D., Fenger, G., Younger-Shepherd, S., Jan, L. -Y. & Jan, Y.-N. Dorsal and ventral cells respond differently to the Notch ligands Delta and Serrate during Drosophila wing development. Genes Dev. 10, 421–434 (1996).
13. de Celis, J. F., Garcia-Bellido, A. & Bray, S. J. Activation and function of Notch at the dorsal-ventral boundary of the wing imaginal disc. Development 122, 359–369 (1996).
14. Irvine, K. & Wieschaus, E. fringe, a boundary specific signalling molecule, mediates interactions between dorsal and ventral cells during Drosophila wing development. Cell 79, 595–606 (1994).
15. Wu, J. Y., Wen, L., Zhang, W. J. & Rao, Y. The secreted product of Xenopus gene lunatic Fringe, a vertebrate signaling molecule. Science 273, 355–358 (1996).
16. Yuan, Y. P., Schultz, J., Mlodzik, M. & Bork, P. Secreted fringe-like signaling molecules may be glycosyltransferases. Cell 88, 9–11 (1997).
17. Amado, M., Almeida, R., Schwientek, T. & Clausen, H. Identification and characterization of large galactosyltransferase gene families: galactosyltransferases for all functions. Biochim. Biophys. Acta 1473, 35–53 (1999).
18. Röttger, S. et al. Localization of three human polypeptide GalNAc-transferases in HeLa cells suggests initiation of O-linked glycosylation throughout the Golgi apparatus. J. Cell Sci. 111, 45–60 (1998).
19. Nilsson, T. & Warren, G. Retention and retrieval in the endoplasmic reticulum and the Golgi apparatus. Curr. Opin. Cell Biol. 6, 517–521 (1994).
20. Breton, C. & Imberty, A. Structure/function studies of glycosyltransferases. Curr. Opin. Struct. Biol. 9, 563–571 (1999).
21. Gastinel, L. N., Cambillau, C. & Bourne, Y. Crystal structures of the bovine β4galactosyltransferase catalytic domain and its complex with uridine diphosphogalactose. EMBO J. 18, 3546–3557 (1999).
22. Harris, R. J. & Spellman, M. W. O-linked fucose and other post-translational modifications unique to EGF modules. Glycobiology 3, 219–224 (1993).
23. Moloney, D. J. & Haltiwanger, R. S. The O-l fucose glycosylation pathway: identification and characterization of a uridine diphosphoglucose: fucose-β1,3-glucosyltransferase activity from Chinese hamster ovary cells. Glycobiology 9, 679–687 (1999).
24. Blaumueller, C. M., Qi, H., Zagouras, P. & Artavanis-Tsakonas, S. Intracellular cleavage of Notch leads to a heterodimeric receptor on the plasma membrane. Cell 90, 281–291 (1997).
25. Logeat, F. et al. The Notch1 receptor is cleaved constitutively by a furin-like convertase. Proc. Natl Acad. Sci. USA 95, 8108–8112 (1998).
26. Goode, S. & Perrimon, N. Brainiac and fringe are similar pioneer proteins that impart specificity to notch signaling during Drosophila development. Cold Spring Harb. Symp. Quant. Biol. 62, 177–184 (1997).
27. Bergemann, A. D., Cheng, H. J., Brambilla, R., Klein, R. & Flanagan, J. G. ELF-2, a new member of the Eph ligand family, is segmentally expressed in mouse embryos in the region of the hindbrain and newly forming somites. Mol. Cell. Biol. 15, 4921–4929 (1995).
28. Amado, M. et al. A family of human β3-galactosyltransferases. Characterization of four members of a UDP-galactose:β-N-acetyl-glucosamine/β-N acetyl-galactosamine β-1,3-galactosyltransferase family. J. Biol. Chem. 273, 12770–12778 (1998).
29. Brückner, K. et al. EphrinB ligands recruit GRIP family PDZ adaptor proteins into raft membrane microdomains. Neuron 22, 511–524 (1999).
30. Stanley, H., Botas, J. & Malhotra, V. The mechanism of Golgi segregation during mitosis is cell type-specific. Proc. Natl Acad. Sci. USA 94, 14467–14470 (1997).

Mice overexpressing human uncoupling protein-3 in skeletal muscle are hyperphagic and lean

John C. Clapham*, Jonathan R. S. Arch*, Helen Chapman*, Andrea Haynes*, Carolyn Lister*, Gary B. T. Moore*, Valerie Piercy*, Sabrina A. Carter*, Ines Lehner*, Stephen A. Smith*, Lee J. Beeley†‡, Robert J. Godden§, Nicole Herrity‖, Mark Skehel¶, K. Kumar Changani#, Paul D. Hockings#, David G. Reid#, Sarah M. Squires#, Jonathan Hatcher☆, Brenda Trail☆, Judy Latcham**, Sohaila Rastan††, Alexander J. Harper☆, Susana Cadenas‡‡, Julie A. Buckingham‡‡, Martin D. Brand‡‡ & Alejandro Abuin†††

Departments of Vascular Biology, † Bioinformatics, § Molecular Biology, ‖ Gene Expression Sciences, ¶ Bioanalytical Sciences, ☆ Neurobehavioiural Research, and †† Comparative Genetics, SmithKline Beecham Pharmaceuticals, Third Avenue, Harlow, Essex, CM19 5AW, UK
Departments of # Safety Assessment and ** Laboratory Animal Sciences, The Frythe, Welwyn, Hertfordshire, AL6 9AR, UK
‡‡ Department of Biochemistry, University of Cambridge, Tennis Court Road, Cambridge, CB2 1QW, UK, and MRC-Dunn Human Nutrition Unit, Hills Road, Cambridge CB2 2XY, UK

Uncoupling protein-3 (UCP-3) is a recently identified member of the mitochondrial transporter superfamily[1,2] that is expressed predominantly in skeletal muscle[1,2]. However, its close relative UCP-1 is expressed exclusively in brown adipose tissue, a tissue whose main function is fat combustion and thermogenesis. Studies on the expression of UCP-3 in animals and humans in different physiological situations support a role for UCP-3 in energy balance and lipid metabolism[3,4]. However, direct evidence for these roles is lacking. Here we describe the creation of transgenic mice that overexpress human UCP-3 in skeletal muscle. These mice are hyperphagic but weigh less than their wild-type littermates. Magnetic resonance imaging shows a striking reduction in adipose tissue mass. The mice also exhibit lower fasting plasma glucose and insulin levels and an increased glucose clearance rate. This provides evidence that skeletal muscle UCP-3 has the potential to influence metabolic rate and glucose homeostasis in the whole animal.

The human α-skeletal actin promoter was used to drive tissue-